Available online at www.sciencedirect.com
SCIENCE DIRECT
Journal of Power Sources 156 (2006) 334–344
JOURNAL OF POWER SOURCES
www.elsevier.com/locate/jpowsour

Computational analysis of heat and mass transfer in a micro-structured PEMFC cathode

S. Litster [a], J.G. Pharoah [a,1], G. McLean [a,b], N. Djilali [a,*]

[a] *Institute for Integrated Energy Systems, University of Victoria, PO Box 3055, Vic., BC, Canada V8W 3P6*
[b] *Angstrom Power Inc., North Vancouver, BC, Canada V7P 3N4*

Received 10 March 2005; received in revised form 18 May 2005; accepted 19 May 2005
Available online 22 July 2005

Abstract

This paper presents a two-dimensional computational model of micro-structured cathodic electrodes featuring nano-porous gas diffusion media that increase the surface to volume ratio of the deposited catalyst layer. A key objective of the modeling effort is to elucidate the Knudsen diffusion within the nano-porous electrode. In addition, the model is non-isothermal and resolves the natural convection in the ambient air directly above the cathode. A major component of the analysis is the identification of mass transport limitations introduced by the micro-structured electrode and the nano-porous gas diffusion layer. Furthermore, the potential for passive regulation of temperature and oxygen supply is investigated. This analysis of the natural convection is unique because it examines buoyancy effects above a horizontal plate with variation in thermal conductivity, segregated regions of porous media, and discrete heating locations. The results of this study indicate that this electrode configuration is feasible and does not suffer from insurmountable mass transfer limitations.

Keywords: PEM fuel cell; Micro-fuel cell; Fuel cell modeling; Nano-pores; Air breathing; Natural convection

1. Introduction

Techno-economic analyses have shown that portable consumer electronics are a more accessible market for fuel cells in the immediate future, in comparison to automobiles, because a much higher cost per unit of energy is acceptable [1]. A key advantage of fuel cells for such applications is the much longer continuous operation and almost instantaneous refueling (as opposed to the recharging time required by batteries). The viability of proton exchange membrane (PEM) fuel cells as battery replacements requires that PEM fuel cells undergo significant miniaturization while achieving higher power densities. This presents challenges for small scale and micro-fuel cells in terms of design, materials, effective transport of reactants, and heat management.

The adaptation of conventional fuel cell designs for smaller applications is restricted by their macroscale materials and manufacturing processes. Exploitation of microscale transport processes in conjunction with macro-manufacturing processes, such as those applied in the production of integrated-circuit chips, make it possible to conceive extremely high power density fuel cells [1]. Such fuel cells have the potential to be significantly cheaper, smaller, and lighter than planar plate and frame fuel cells; they could also broaden the range of fuel cell applications.

The implementation of thin layer manufacturing processes can effectively reduce stack size and conductive path length, both of which enhance volumetric power density. Microfabrication of flow fields, current collectors, and electrical interconnects has been reported in the literature [2–4]. However, these fuel cell designs have generally relied on traditional planar MEA architecture. Because the majority of PEM fuel cell designs are based on planar plate and frame architecture, their volumetric power densities are inherently constrained by their two-dimensional active area. Non-planar

* Corresponding author. Tel.: +1 250 721 6034; fax: +1 250 721 6323.
E-mail address: ndjilali@uvic.ca (N. Djilali).
[1] Current address: Department of Mechanical Engineering, Queens University at Kingston, Kingston, Ont., Canada.

0378-7753/$ – see front matter © 2005 Elsevier B.V. All rights reserved.
doi:10.1016/j.jpowsour.2005.05.064

Nomenclature

C_p	specific heat ($J\,kg^{-1}\,K^{-1}$)
d_{por}	pore diameter (m)
D	diffusion coefficient ($m^2\,s^{-1}$)
F	Faraday's constant ($96\,485\,C\,mol^{-1}$)
$\mathbf{g}$	gravity vector ($m\,s^{-2}$)
h	height (m)
h	static enthalpy ($J\,kg^{-1}$)
$\bar{h}$	mean heat transfer coefficient
H	total enthalpy ($J\,kg^{-1}$)
i	local current density ($A\,m^{-2}$)
I	average current density ($A\,m^{-2}$)
k	permeability (m^2)
M	molar mass ($kg\,mol^{-1}$)
n_{e^-}	number of electrons transferred (–)
Nu	Nusselt number (–)
P	pressure (Pa)
Pr	Prandtl number (–)
q	heat flux ($W\,m^{-2}\,K^{-1}$)
R	universal gas constant ($8.3145\,J\,mol^{-1}\,K^{-1}$)
Ra	Rayleigh number (–)
Δs	entropy change ($J\,mol^{-1}\,K^{-1}$)
$\dot{S}$	source term
T	temperature (K)
$\mathbf{u}$	velocity vector ($m\,s^{-1}$)
w	width (m)
W	width of fuel cell (m)
x	local horizontal position (m)
X	global horizontal position (m)
y	local vertical position (m)
y	mass fraction (–)
Y	global vertical position (m)

Greek letters

β	thermal expansion coefficient
ε	porosity (–)
η	over-potential (V)
λ	thermal conductivity ($W\,m^{-1}\,K^{-1}$)
μ	viscosity ($kg\,m\,s^{-1}$)
ν	kinematic viscosity ($m^2\,s^{-1}$)
ρ	density ($kg\,m^{-3}$)
τ	tortuosity factor (–)
ϕ	mixture quantity (–)

Subscripts

H	heat
i	species index
Kn	Knudsen quantity
nc	natural convection region
p	porous region
s	solid region

designs can achieve much higher active area to volume ratios, and hence higher volumetric power densities; this was demonstrated in the waved cell topology proposed by Mérida et al. [5] in which a waved membrane-electrode assembly was supported by an expanded metallic mesh structure. In this design, the MEA played an additional function by forming the channels that distribute the fuel and oxidant. Thus, the volume that previously comprised the flow channels could support additional active area and generate increased volumetric power density. In practice, however, the pitch of the MEA undulations is limited by conventional fabrication techniques.

Another approach for increasing the volumetric power density of a fuel cell power supply is to reduce the number of ancillary devices. In low-power applications, such as portable consumer electronics, fuel cells can operate effectively in a passive air-breathing mode [2,4,6–8]. Oxygen is supplied to the cathode by natural convection currents induced by the temperature difference between an operating fuel cell and the ambient air. The natural convection eliminates the requirement of manifolding, fans, and compressors for the oxidant stream. However, passive air-breathing cells are limited to single-plane configurations because of the requirement of an unobstructed cathode surface [2,3,6,7]. In some cases, a 'side-by-side' series connection of individual fuel cells has been adopted to achieve greater voltages [2,3]. The literature indicates that passive air-breathing fuel cells developed to date appear to become mass transfer limited at current densities between 0.15 and $0.35\,mA\,cm^{-2}$ [2,4,7]. This is due to the reduced (atmospheric) pressure of the oxidant, instead of the 3–5 atm typically employed, as well as the reduced convective transport capacity.

1.1. Computational fuel cell modeling

Computational fuel cell models are valuable tools for designing and optimizing fuel cells, as well as for enhancing the fundamental understanding of the multi-physics phenomena present in a fuel cell. These phenomena include multi-component fluid, ionic, electronic and thermal transport, all coupled with electrochemical reactions taking place in a variety of media, including porous gas diffusion electrodes. The corrosive and electrical environment in a fuel cell complicates the process of acquiring in situ measurements, further increasing the value of computational modeling.

Due to the high activation energy required for the oxygen reduction reaction (ORR) and the required water management due to condensation, the cathode has been of particular interest in previous computational modeling efforts [9–19]. Two-dimensional cathode-side only models have been developed by Wang et al. [18] and by You and Liu [19]. The significant distinction between these two models is that Wang et al. treated the cathode catalyst layer as an infinitely thin surface of reaction; in contrast, You and Liu employed a pseudo-homogeneous model of a finite thickness catalyst layer. Entire unit cells have been modeled in three-dimensions with the additional complexity of membrane transport and

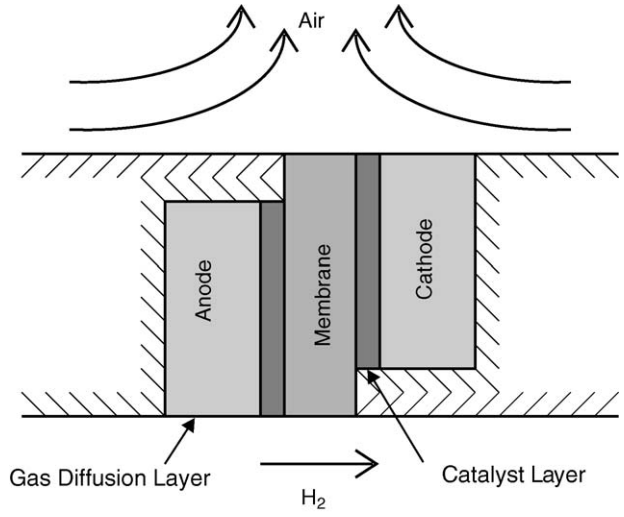

Fig. 1. Schematic of the micro-structured electrode. The electrode coordinate system (x, y) is indicated in the lower left corner.

phase potential [11], as well as two-phase transport in both cathode and anode diffusion layer [10,16]. However, the additional governing equations and the expanded dimensions result in a model that requires significant computational resources.

1.2. Present study

This paper introduces a novel micro-structured PEMFC electrode that exploits the principles discussed above and presents results from a computational analysis of this patented design [20–22]. The non-planar, air-breathing, and micro-structured electrode is shown schematically in Fig. 1. In this electrode, gases must traverse the catalyst layer as they diffuse through the nano-porous GDL in a path parallel to the active area.

The micro-structured electrodes employ a nano-porous GDL featuring a mean pore diameter on the order of 100 nm. The mean pore diameter in typical non-woven GDLs is between 100 and 500 times greater than those considered herein. By maintaining comparative levels of porosity, the nano-porous GDL increases the active area of the deposited catalyst by exploiting the surface to volume ratio [1]. State of the art thin-film catalyst layers [23] bound by Nafion ionomer are attached either to the carbon-fiber backing layer or the PEM. By employing a nano-porous GDL, the catalyst can be directly deposited into the pores of the GDL. However, the high functionality of the nano-porous GDL comes at the cost of reduced diffusion rates.

Two possible obstacles to the feasibility of this design to operate at practical volumetric power densities were identified:

1. The ability of nano-scale porous media to effectively transport reactant and product gases to the entire active area.
2. The ability of natural convection to passively regulate temperature and supply adequate amounts of oxygen to the cathode.

A computational model was developed to undertake an analysis of the micro-structured electrodes in order to assess the functionality of this design, determine the severity of potential transport limitations, and identify design parameters to alleviate such problems.

2. Model description

The model presented herein is a two-dimensional representation of three micro-structured cathodic electrodes placed in close proximity. The computational domain, shown schematically in Fig. 2, encompasses the cathodic electrodes and the region of natural convection above the electrodes. A solid region between each electrode is included to facilitate the heat transfer modeling. In Fig. 2, the global coordinate system (X, Y) is depicted. The transport phenomena considered in the model include:

- diffusive transport of the reactant and product species;
- convective heat and mass transfer driven by density variation in the natural convection region;
- Knudsen diffusion through the cathode GDL;
- electrochemical reactions;
- conjugate heat transfer.

The large variation of length scales and the highly complex and coupled nature of the phenomena found in this system requires a number of assumptions in order to develop a numerically tractable model. The assumptions contained in the present model include:

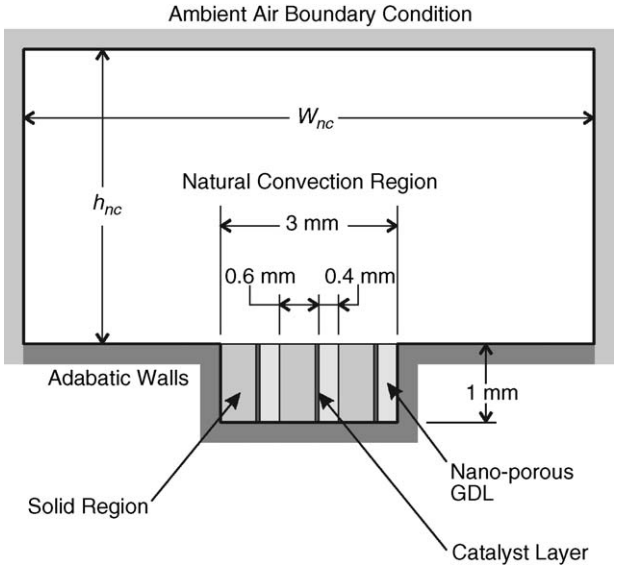

Fig. 2. Two-dimensional computation domain and relevant dimension. The global coordinate system (X, Y) is indicated in the lower left corner of the natural convection region.

1. The phenomena present are primarily two-dimensional.
2. Steady-state conditions predominate in the fuel cell and in the natural convection region.
3. The porous media is isotropic and homogeneous.
4. The gases are compressible and ideal.
5. The flow in the natural convection region is laminar.
6. Knudsen diffusion is the dominant mode of mass transfer in the GDL.
7. The transport of reactants and water through the electrolyte is negligible.
8. The activation over-potential in the cathode catalyst layer is constant and uniform.
9. Water exists in vapour form only.
10. The catalyst layer is an interface.
11. Additional fuel cell components are represented by a solid with a representative thermal conductivity.
12. Heat transfer from the fuel cell is solely through the natural convection on the air side of the fuel cell.

The effect of surface curvature on liquid water's vapor pressure in hydrophobic porous materials supports the assumption of zero liquid water (Assumption 9). Since PEM fuel cell gas diffusion layers are hydrophobic, water droplets form a convex surface against the gas phase due to contact angles greater than 90°. This surface curvature generates a higher pressure in the liquid phase, increasing the transfer of the condensed phase and corresponding to accelerated evaporation [24]. Nevertheless, even if the liquid phase was perfectly wetting, meaning a contact angle of 0°, the Kelvin equation predicts that the concave interface would only decrease the saturation pressure by 1.3% for the present average pore diameter of 65 nm [24].

2.1. Model equations

2.1.1. Mixture properties

In the following description of the model, the properties of the gas are mixture quantities determined from the composition of the gas and the temperature. The mixture quantities ϕ of viscosity μ, static enthalpy h, and thermal conductivity λ are determined from the mass fraction y_i of each species by:

$$\phi = \sum y_i \phi_i \tag{1}$$

The density ρ is resolved by the ideal gas assumption in which the density of each species is expressed as:

$$\rho_i = \frac{PM_i}{RT} \tag{2}$$

where P is the pressure, M the molecular mass, R the universal gas constant, and T is the temperature. The mixture density is related to each species density and its mass fraction:

$$\frac{1}{\rho} = \sum \frac{y_i}{\rho_i} \tag{3}$$

2.1.2. Natural convection region

The transport equations solved in the ambient air include continuity, momentum, energy and mass transport equations. The continuity equation is expressed as:

$$\nabla \cdot (\rho \mathbf{u}) = 0 \tag{4}$$

where $\mathbf{u}$ is the mixture velocity. The momentum equation is defined as:

$$\nabla \cdot (\rho \mathbf{u} \otimes \mathbf{u}) = \rho \mathbf{g} - \nabla \cdot \left(P\delta + \frac{2}{3}\mu \nabla \cdot \mathbf{u} \right) + \nabla \cdot (\mu (\nabla \cdot \mathbf{u})^{\mathrm{T}}) \tag{5}$$

where $\mathbf{g}$ is the gravity, P the mixture hydrodynamic pressure, and δ the Kronecker delta. Buoyancy effects, due to variation in temperature and composition, are introduced implicitly by ideal gas law and the gravity vector. The energy equation is expressed as:

$$\nabla \cdot (\rho \mathbf{u} H - \lambda \nabla T) = 0 \tag{6}$$

where H is the total enthalpy. The total enthalpy is the sum of the static enthalpy and the kinetic energy:

$$H = h + \frac{1}{2}\mathbf{u}^2 \tag{7}$$

The mass transport equation is articulated as:

$$\nabla \cdot (\rho \mathbf{u} y_i) - \nabla \cdot (D_i \nabla y_i) = 0 \tag{8}$$

where y_i and D_i are the mass fraction and molecular diffusion coefficient of the ith species, respectively.

2.1.3. Gas diffusion layer

The transport equations in the porous GDL have been formulated for the Knudsen diffusion regime. In the GDL, the conservation equation is unchanged, whereas the momentum equations are reformulated as Darcy's law for porous media:

$$\mathbf{u} = \frac{k_{\mathrm{Kn}}}{\mu} \nabla P \tag{9}$$

where k_{Kn} is the Knudsen pseudo-permeability that is derived in Appendix A. The distinction between pressure and species-gradient driven Knudsen diffusion has been adopted from the work of Kast and Hohenthanner [25]. The Knudsen pseudo-permeability represents the portion of the Knudsen flux driven by the gradient of pressure and is expressed as:

$$k_{\mathrm{Kn}} = \frac{4}{3}\frac{\varepsilon}{\tau}\frac{\mu d_{\mathrm{por}}}{P}\sqrt{\frac{RT}{2\pi}} \sum \frac{y_i}{\sqrt{M_i}} \tag{10}$$

where ε is the porosity, τ the tortuosity factor, and d_{por} the mean pore diameter. This pseudo-permeability is several orders of magnitude ($k_{\mathrm{Kn}} \approx 1 \times 10^{-16}\,\mathrm{m}^2$) less than that of typical fibrous GDLs. The mass transport equation in the porous GDL is modified for diffusion through the nano-porous substrate by the inclusion of an effective Knudsen

diffusivity $D^{\text{eff}}_{i,\text{Kn}}$ and a source/sink term $\dot{S}_i$ that accounts for the electrochemistry:

$$\nabla \cdot (\rho \mathbf{u} y_i) - \nabla \cdot (D^{\text{eff}}_{i,\text{Kn}} \nabla y_i) = \dot{S}_i \tag{11}$$

The Knudsen diffusivity $D_{i,\text{Kn}}$ is corrected for the geometry of the porous media by the porosity ε and the tortuosity factor τ

$$D^{\text{eff}}_{i,\text{Kn}} = \frac{\varepsilon}{\tau} D_{i,\text{Kn}} \tag{12}$$

The Knudsen diffusivity is derived from kinetic theory and is expressed as:

$$D_{i,\text{Kn}} = \frac{4}{3} d_{\text{por}} \sqrt{\frac{RT}{2\pi M_i}} \tag{13}$$

The energy equation is modified in the GDL by the inclusion of a reaction heating term $\dot{S}_\text{H}$ and the introduction of an effective thermal conductivity λ_{eff}

$$\nabla \cdot (\rho \mathbf{u} H - \lambda_{\text{eff}} \nabla T) = \dot{S}_\text{H} \tag{14}$$

The effective thermal conductivity is determined volumetrically by:

$$\lambda_{\text{eff}} = (1 - \varepsilon)\lambda_\text{p} + \varepsilon\lambda \tag{15}$$

where λ_p is the thermal conductivity of the porous matrix.

2.1.4. Solid region

In the solid region, which represents additional fuel cell components, the energy equation is the only equation solved. The energy equation simply accounts for conduction and is expressed as:

$$\nabla \cdot (\lambda_\text{s} \nabla T) = 0 \tag{16}$$

where λ_s is the conductivity of the solid region. This conductivity is lower than that of the porous matrix λ_p to adequately represent the non-resolved fuel cell components.

2.1.5. Catalyst layer

The cathode catalyst layer is where the oxygen reduction reaction is located and is modeled as an interface. The modeling of the electrochemistry is simplified by assuming a first-order reaction dependent on oxygen and by the assumption of uniform activation overpotential. The local current density i is determined from a specified average current density I. In addition, the assumption of uniform activation over-potential results in the local current density being dependent only on the local oxygen concentration. Thus, the local current density is resolved by the ratio of local oxygen concentration to the average oxygen concentration along the entire catalyst layer:

$$i = I \frac{y_{\text{O}_2}}{y^{\text{ave}}_{\text{O}_2}} \tag{17}$$

The local oxygen sink term is expressed as:

$$\dot{S}_{\text{O}_2} = -\frac{M_{\text{O}_2}}{4F} i \tag{18}$$

where F is the Faraday constant, and i is the local current density. The source for the water vapor is calculated with a similar expression:

$$\dot{S}_{\text{H}_2\text{O}} = \frac{M_{\text{H}_2\text{O}}}{2F} i \tag{19}$$

Additionally, the source of heat in the catalyst is defined as [26]:

$$\dot{S}_\text{H} = \left[\frac{T(-\Delta s)}{F(n_{\text{e}^-})} + \eta \right] i \tag{20}$$

where Δs is the entropy change for the reaction, n_{e^-} is the number of electrons transferred, and η is the term representing the activation overpotential and ohmic losses.

2.2. Boundary conditions

The boundary conditions at the top and side walls, adjacent to the natural convection region, are specified to depict static ambient air. Thus, the velocity is set to zero:

$$\mathbf{u} = 0$$

the temperature is set to the ambient level:

$$T = 293\,\text{K}$$

the pressure is set to the ambient:

$$P = 101\,325\,\text{Pa}$$

and the mass fractions y_i are set to that of ambient air for a specified relative humidity of 80%.

The bottom walls of the natural convection region and the bottom and sides of the fuel cell are adiabatic:

$$\frac{\partial T}{\partial n} = 0$$

and feature zero species flux:

$$\frac{\partial y_i}{\partial n} = 0$$

2.3. Modeling parameters

The results presented herein are for the three-cell stack configuration of the micro-structured fuel cell. The electrode aspect ratio is 2.5. Table 1 lists the dimensions of the geometry considered.

The operating conditions of the cell have been chosen to represent a micro-structured fuel cell operating as a power supply for a small portable electronic device. Thus, the ambient boundary condition was applied to represent a typical ambient environment. In addition, the average current density of 200 mA cm^{-2} was specified to provide results in the

Table 1
Geometry

Dimension	Value
Height of GDL, h_{GDL} (mm)	1.0
Width of GDL, w_{GDL} (mm)	0.4
Width of solid regions, w_s (mm)	1.0
Height of natural convection region, h_{nc} (mm)	18.0
Width of natural convection region, w_{nc} (mm)	39.0

Table 2
Operating conditions

Property	Value
Ambient pressure, P_a (atm)	1
Ambient temperature, T_a (K)	293
Ambient relative humidity, ϕ (%)	80
Ambient O_2 mass fraction, $y_{O_2,a}$	0.2303
Ambient H_2O mass fraction, $y_{H_2O,a}$	0.0115
Average current density, I (mA cm^{-2})	200
Entropy generation, Δs J (kg^{-1} K^{-1}) [26]	−326
Activation overpotential, η (V)	0.25

Table 3
Material properties

Property	Value
Porosity of GDL, ε	0.45
Tortuosity factor of the GDL, τ [29]	3
Mean pore diameter of GDL, d_{por} (nm)	65
Thermal conductivity of the porous regions, λ_p (W m K^{-1}) [28]	1.0
Thermal conductivity of the solid regions, λ_s (W m K^{-1})	0.64

region of mass transfer limitations for an air-breathing fuel cell. Table 2 presents the values of the operating conditions.

The material properties (see Table 3) have been chosen to represent the anticipated use of the nano-porous substrate. These materials are characterized by pore diameters on the order of tens of nanometers and low to moderate thermal conductivity. A porosity of 0.45 for the nano-porous GDL is assumed, which is in-line with other low-porosity GDL materials [27]. The thermal conductivity of a nano-porous GDL is assumed to equal that of graphite powder (1.0 W m K^{-1}) [28]. The thermal conductivity of the solid region is reduced below that of the nano-porous GDL to reflect the relatively low thermal conductivity of polymer electrolyte membrane.

2.4. Computational procedure

The governing equations are solved using CFX v4.3. This computational fluid dynamics (CFD) code uses the finite volume method. The equations were discretized with a higher-order upwind differencing scheme and the pressure correction was achieved with the SIMPLEC algorithm. The numerical solution was obtained by employing the algebraic multi-grid method. The structured computational grid employed is depicted in Fig. 3. The open-air region grid size is [300 × 100], and the grid size of each electrode is [20 × 29].

Fig. 4 presents a magnified view of the computational mesh for the micro-structured fuel cell. This plot and the previous plot of the computational mesh highlight the disparity between length scales within the model. A significant effort has been made to develop an efficient grid that provides a grid independent solution.

3. Results and discussion

3.1. Analysis of the natural convection

The natural convection induced by the micro-structured fuel cell is similar to natural convection above horizontal plates that has been studied experimentally in the literature [30–34]. In addition to experimental studies, natural convection from upward facing horizontal plates has been studied numerically [32,33]. Martorell et al. [32] studied the application of natural convection to the cooling of printed circuit boards in a computational manner similar to that used in the present study. Their study represented heating components on printed circuit boards as narrow and semi-infinite plates and

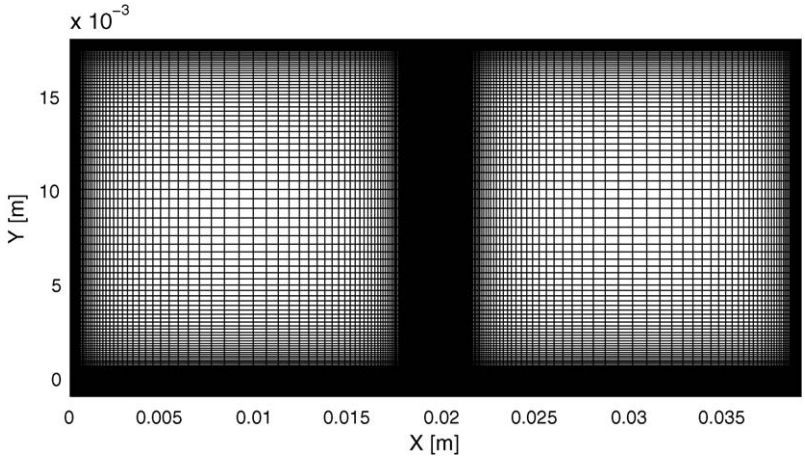

Fig. 3. Computational mesh for both the natural convection region and micro-structured fuel cell.

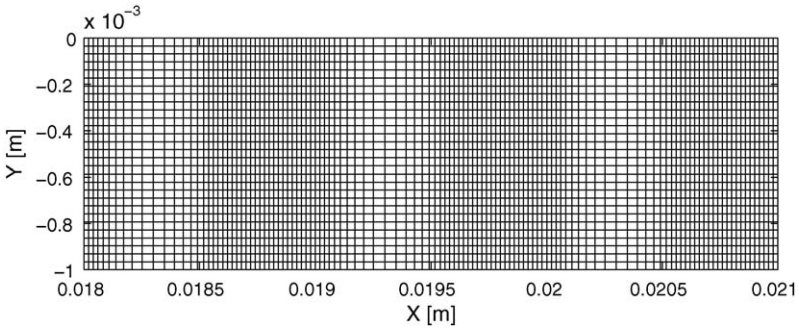

Fig. 4. Computational mesh for the micro-structured electrodes and solid regions. The plot is dimensioned with the global coordinate system.

were thus amenable to a two-dimensional analysis. They also conducted a three-dimensional computational investigation of natural convection above a 6.0 cm × 23.0 cm horizontal plate. The results indicated no significant change in the heat transfer from the two-dimensional simulation.

In order to accurately model the natural convection above the micro-structured electrodes, a study of the dependence of the heat transfer from the micro-structured fuel cell on the size of the natural convection region was required. The solution, particularly the temperature in the porous region, was found to be sensitive to the domain size. For domain sizes larger than 18 mm, the effect on the temperature in the cathode was negligible. In all domain sizes investigated, the mass transfer within the cathode was independent of the domain size.

The feasibility of supplying oxygen to a PEM fuel cell electrode through natural convection was evaluated theoretically by Li et al. [8]. They considered natural convection driven strictly by gradients in concentration instead of temperature. Their results were obtained using empirical heat transfer correlations adapted for mass transfer. In order to quantify the relative effect of this form of natural convection, the ratio of change in density due to the predicted mean difference in temperature the between surface and ambient ($\Delta\bar{\rho}_T$) to that due to the mean difference in mass fractions between the surface and ambient ($\Delta\bar{\rho}_y$) was evaluated. With the ideal gas law, the ratio can be expressed as:

$$\frac{\Delta\bar{\rho}_T}{\Delta\bar{\rho}_y} = \frac{1 - T_a/T_s}{1 - M_s/M_a} = 25.6 \tag{21}$$

where the subscripts a and s represent ambient and average surface quantities respectively. The ratio of 25.6 clearly indicates that, for the conditions considered herein, the concentration gradient has a negligible effect on the natural convection. This conclusion facilitates a comparison between the present results and those found in the literature for horizontal plates.

The Rayleigh number Ra (the ratio between buoyancy and heat advection to viscous forces and heat conduction) for this study is 124. Herein, the Rayleigh number employs the width of the electrodes and solid regions ($W = 3$ mm) as the characteristic length and is formulated as:

$$Ra = \frac{g\beta C_p}{\mu\lambda}\Delta T W^3 \tag{22}$$

where β is the thermal expansion coefficient and C_p is the specific heat. The average Nusselt number was calculated and found to be 1.90 using the relationship:

$$Nu = \frac{\bar{h}W}{\lambda} \tag{23}$$

where

$$\bar{h} = \frac{q}{\bar{T}_s - T_a} \tag{24}$$

The Nusselt number for the micro-structured fuel cell was then compared to a number of correlations for heat transfer from upwards facing horizontal plates. Table 4 lists the range of Nusselt numbers obtained in the literature for the Rayleigh number presently considered. Reasonable agreement is shown in the table considering the correlations listed do not explicitly account for discrete regions of heating, conductivity variation, and porous media.

Further validation of the heat transfer predicted for the micro-structured fuel cell was obtained by comparing local Nusselt numbers with those of an analytical expression presented by Sparrow and Carlson [34]. The analytical expression is resolved for a uniform heat flux boundary condition and a Prandtl number Pr of 0.7. The expression employs a modified Rayleigh number Ra^*, expressed as:

$$Ra^* = \frac{g\beta q_x W^4}{\nu^2\lambda} Pr \tag{25}$$

The analytical solution to the local Nusselt number is articulated as [34]:

$$\frac{Nu}{(Ra^*)^{1/6}} = \frac{0.553}{(x/W)^{1/3}} \quad \left(0 \le x \le \frac{W}{2}\right) \tag{26}$$

Table 4
Comparison of the average Nusselt number of the micro-structured fuel cell with heat transfer correlations for horizontal plates in the literature

Source	Nusselt number ($Ra = 124$)
Present study	1.90
Fishenden and Saunders [30]	1.80
Fujii and Imura [31]	0.80
Martorell et al. [32]	2.83
Sparrow and Carlson [34]	2.39

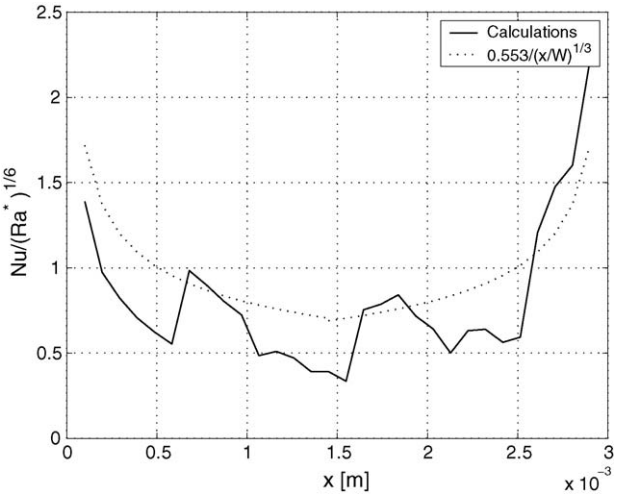

Fig. 5. Comparison of the local Nusselt number for the micro-structured cell with the analytical solution for a semi-infinite uniformly heated plate.

Fig. 5 presents profiles of the local Nusselt number obtained with the computational model of the micro-structured fuel cell and that of the analytical expression for uniform heat flux. The influence of discrete heating and conductivity variance is evident, but a general agreement with the analytical expression is obtained.

Fig. 6 presents isothermal lines in both the natural convection region and the micro-structured fuel cell. The thermal plume is similar in structure to those resolved by Pretot et al. [33] and Martorell et al. [32]. The corresponding vectors of velocity are shown in Fig. 7. The velocity vectors and isotherms indicate significant heating of the air as it travels along the surface of the adiabatic wall towards the micro-structured electrode. In addition, the stagnation of the flow at the mid-point of the cathode surface is evident in the velocity vectors.

Fig. 8 depicts the influence of the heating of the approaching air and the stagnation point on the surface temperature of the micro-structured cathode. The figure also indicates artifacts of the discrete heating from the individual catalyst layers and the variation of thermal conductivity. Typically, the maximum surface temperature on horizontal plates is located at the stagnation point in the centre of the plate. The stagnation point corresponds to a location of $x = 1.48$ mm on the

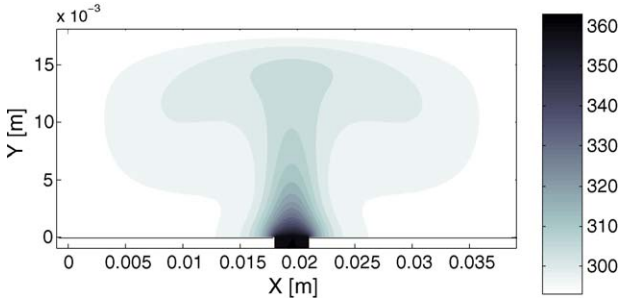

Fig. 6. Temperature distribution (K).

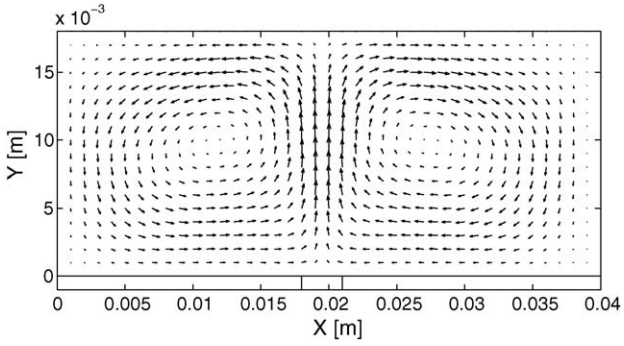

Fig. 7. Vectors of velocity in the natural convection region. Maximum velocity of 0.0627 m s^{-1}.

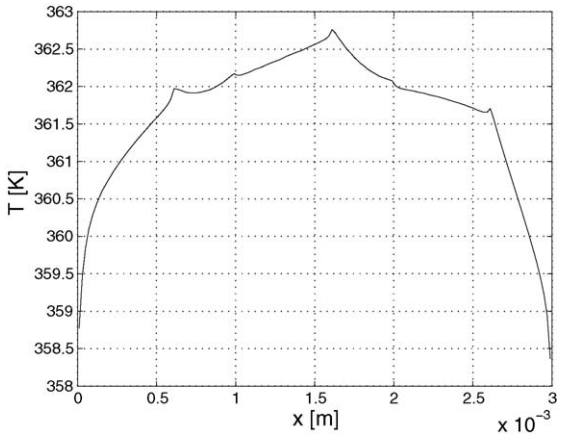

Fig. 8. Temperature profile over the surface of the micro-structured fuel cell ($Y = 0$). The ambient temperature is 293 K.

cell; however, the maximum surface temperature is located at $x = 1.61$ mm. The latter location is that of the central catalyst layer, indicating the significant influence of the discrete heating on the temperature field.

3.2. Analysis of the fuel cell

Fig. 9 illustrates the temperature distribution predicted within the micro-structured fuel cell. As anticipated, the highest temperature gradients are located at the upper left and right corners where the greatest Nusselt numbers were obtained. In addition, there is a significant amount of transverse conduction as a result of the heating along each vertical catalyst

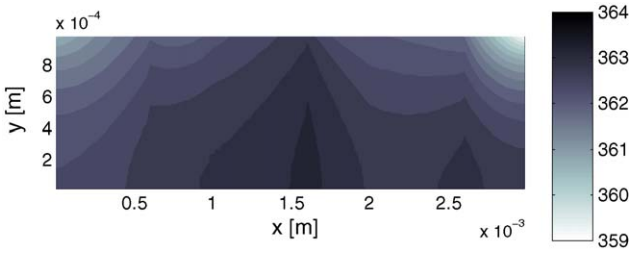

Fig. 9. Temperature distribution in the micro-structured electrodes and solid regions (K). The ambient temperature is 293 K.

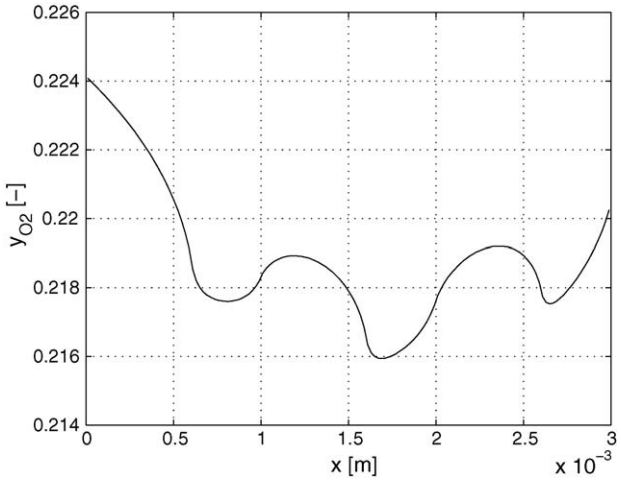

Fig. 10. Oxygen mass fraction profile over the surface of the micro-structured fuel cell ($Y=0$). The ambient oxygen mass fraction is 0.2303.

layer. The maximum temperature predicted inside the cell was 363.3 K. Although this temperature is approximately 10–30 °C higher than typical PEMFC operating temperatures, it is not a serious concern as the model is prone to over-predicting temperature. The over-prediction is because of the adiabatic boundary condition on the sides and bottom of the fuel cell.

The mass transfer results indicate that there is an insignificant reduction in the oxygen concentration at the surface of the electrodes ($Y=0$). The average oxygen mass fraction along the surface of the fuel cell was found to be 0.219. This is only a 5% decrease from the ambient value. Fig. 10 depicts the profile of the oxygen mass fraction over the surface of the micro-structured fuel cell ($Y=0$). The oxygen diffusing into the electrode has a discernible effect on the oxygen mass fraction, but it is not significant.

Fig. 11 illustrates the distribution of oxygen within the three nano-porous electrodes. The catalyst layer is located along the left hand vertical axis for each electrode. A minimum oxygen mass fraction of 0.089, a 61% drop from the ambient, was obtained in the central cathode. The non-linear drop in concentration along the vertical length of the electrode is the result of oxygen consumption along the diffusion pathway. Although the reduction in oxygen concentration is significant, the fuel cell is still far from being starved of oxygen. Thus, the suspected obstacles to feasibility, though not trivial, are not insurmountable. It is also evident that there is little difference in oxygen distribution between the three cells. This shows that additional electrodes would not significantly hinder oxygen transport to the catalyst layers.

The contours of percent relative humidity in Fig. 12 support the assumption that no liquid water exists in the system. The maximum relative humidity resolved was 27.1%, far below the saturation level indicating rapid evaporation. The maximum relative humidities are located at the bottom of the nano-porous cavities and adjacent to the catalyst layer. The low relative humidities, in comparison to the ambient, result from the elevated temperature within the fuel cell that increases the saturation pressure of the water. However, the relative humidity increases with cavity depth due to the production of water at the catalyst layer.

The results of the simulations demonstrate that the micro-structured nano-porous electrode prevails over the two suspected obstacles to feasibility (see Section 1.2). First, the results established that the nano-porous diffusion media sufficiently exchanges the reactant and product gases between the catalyst layer and the ambient air. In addition, the natural convection induced by the reaction heating was proven to provide ample amounts of oxygen at the specified operating point. Moreover, it was established that natural

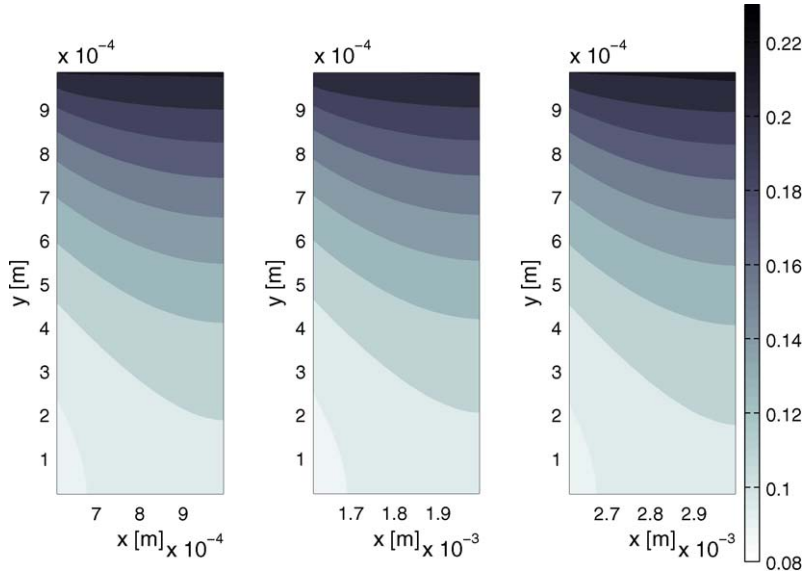

Fig. 11. Mass fraction distribution of oxygen in the three cathodes. The ambient oxygen mass fraction is 0.2303.

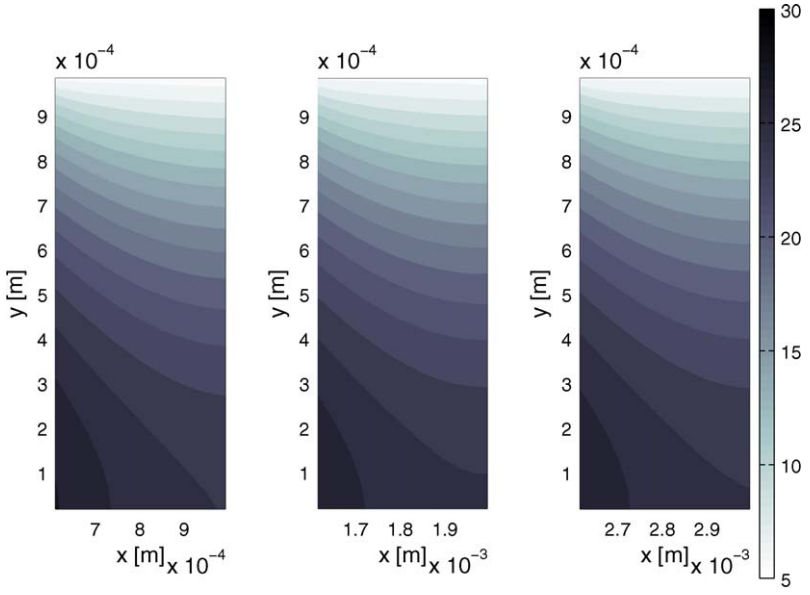

Fig. 12. Percent relative humidity distribution in the three cathodes. The ambient relative humidity is 80%.

convection could be employed to passively cool fuel cells in small portable electronics.

4. Conclusion

A computational model of the cathodic electrodes in ambient air-breathing, non-planar, micro-structured PEMFC was developed. The model was employed to evaluate the feasibility of these electrodes for use in fuel cells to power small portable consumer electronics. Emphasis was placed on the modeling of gas transport through the nano-porous electrode. Expressions for both species and pressure gradient driven Knudsen diffusion were introduced to elucidate possible mass transport limitations. Attention was also paid to the natural convection above the electrodes to determine if it adequately regulates temperature and supplies reactant gases. The results of the analysis demonstrated that this novel electrode is a viable alternative to conventional PEM fuel cell electrodes.

Acknowledgement

This work was funded through a collaborative research agreement with Angstrom Power Inc.

Appendix A

The following appendix contains the derivation of the expressions used to model the Knudsen diffusion through the nano-porous electrode. The mass flux of each species in the Knudsen regime is driven by the partial pressure gradient. Thus, for an isothermal ideal gas the Knudsen mass flux $\mathbf{n}_{\mathrm{Kn}}$ can be presented with the gradient of the species density:

$$\mathbf{n}_{i,\mathrm{Kn}} = -D^{\mathrm{eff}}_{i,\mathrm{Kn}} \nabla \rho_i \tag{27}$$

The mass concentration gradient can be expanded into two terms:

$$\mathbf{n}_{i,\mathrm{Kn}} = -D^{\mathrm{eff}}_{i,\mathrm{Kn}} (\rho \nabla y_i + y_i \nabla \rho) \tag{28}$$

with the inclusion of the ideal gas law, it becomes:

$$\mathbf{n}_{i,\mathrm{Kn}} = -D^{\mathrm{eff}}_{i,\mathrm{Kn}} \rho \nabla y_i - D^{\mathrm{eff}}_{i,\mathrm{Kn}} y_i \frac{M_{\mathrm{Air}} \nabla P}{RT} \tag{29}$$

It can be seen that the diffusion is a function of both the pressure and mass fraction gradients. Presently, we neglect the temperature gradient since preliminary results indicated small temperature gradients in the porous media. The above flux term is now broken down into a mass fraction driven $\mathbf{n}^{y}_{\mathrm{Kn}}$ and a pressure driven $\mathbf{n}^{P}_{\mathrm{Kn}}$ Knudsen flux

$$\mathbf{n}_{\mathrm{Kn}} = \mathbf{n}^{y}_{\mathrm{Kn}} + \mathbf{n}^{P}_{\mathrm{Kn}} \tag{30}$$

The first term on the RHS is the species gradient driven Knudsen diffusion and is given by:

$$\mathbf{n}^{y}_{i,\mathrm{Kn}} = -D^{\mathrm{eff}}_{i,\mathrm{Kn}} \rho \nabla y_i \tag{31}$$

The pressure driven Knudsen diffusion of each species is expressed as:

$$\mathbf{n}^{P}_{i,\mathrm{Kn}} = -D^{\mathrm{eff}}_{i,\mathrm{Kn}} y_i \frac{M_{\mathrm{Air}} \nabla P}{RT} \tag{32}$$

In addition, the bulk pressure driven flux can be achieved by summing the pressure driven flux over all the species

$$\mathbf{n}^{P}_{\mathrm{Kn}} = \sum \mathbf{n}^{P}_{i,\mathrm{Kn}} = -\left(\sum D^{\mathrm{eff}}_{i,\mathrm{Kn}} y_i \right) \frac{M_{\mathrm{Air}} \nabla P}{RT} \tag{33}$$

In order to accommodate the constraints of implementing Knudsen flow in a commercial CFD package, Eq. (A.7) will be arranged in the form of Darcy's law, which is typically formulated as:

$$\mathbf{u} = \frac{k}{\mu}\nabla P \tag{34}$$

where k is the hydraulic permeability. Eq. (33) is converted from a mass flux to a velocity by dividing it by the ideal gas expression for density:

$$\mathbf{u} = -\frac{\sum D_{i,\mathrm{Kn}}^{\mathrm{eff}} y_i}{P}\nabla P \tag{35}$$

A Knudsen pseudo-permeability, which can be employed in the equation for Darcy's law, is obtained by equating Eqs. (34) and (35) and including the expression for effective Knudsen diffusivity (Eqs. (12) and (13)):

$$k = k_{\mathrm{Kn}} = \frac{\mu \sum D_{i,\mathrm{Kn}}^{\mathrm{eff}} y_i}{P} = \frac{4}{3}\frac{\varepsilon}{\tau}\frac{\mu d_{\mathrm{por}}}{P}\sqrt{\frac{RT}{2\pi}}\sum \frac{y_i}{\sqrt{M_i}} \tag{36}$$

Thus, Darcy's law in a commercial CFD package can be employed for modeling the pressure driven Knudsen flux with the following expression:

$$\mathbf{u} = \frac{k_{\mathrm{Kn}}}{\mu}\nabla P \tag{37}$$

References

[1] G. McLean, N. Djilali, M. Whale, T. Niet, Application of micro-scale techniques to fuel cell systems design, in: Proceedings of the 10th Canadian Hydrogen Conference, Quebec City, 2000.

[2] R. Hahn, S. Wagner, A. Schmitz, H. Reichl, Development of a planar microfuel cell with thin film and micropatterning technologies, J. Power Sources 131 (2004) 73–78.

[3] S.J. Lee, A. Chang-Chien, S.W. Cha, R. O'Hayre, Y.I. Park, Y. Saito, F.B. Prinz, Design and fabrication of a microfuel cell array with flip–flop interconnection, J. Power Sources 112 (2002) 410–418.

[4] J.S. Wainright, R.F. Savinell, C.C. Liu, M. Litt, Microfabricated fuel cells, Electrochim. Acta 48 (2003) 2869–2877.

[5] W.R. Mérida, G. McLean, N. Djilali, Non-planar architecture for proton exchange membrane fuel cells, J. Power Sources 102 (2001) 178–185.

[6] D. Chu, R. Jiang, Performance of polymer electrolyte membrane fuel cell (PEMFC) stacks. Part I. Evaluation and simulation of an air-breathing PEMFC stack, J. Power Sources 83 (1999) 128–133.

[7] T. Hottinen, M. Mikkola, P. Lund, Evaluation of planar free-breathing polymer electrolyte membrane fuel cell design, J. Power Sources 129 (2004) 68–72.

[8] P.W. Li, T. Zhang, Q.M. Wang, L. Scharfer, M.K. Chyu, The performance of PEM fuel cells fed with oxygen through the free-convection mode, J. Power Sources 114 (2003) 63–69.

[9] T. Berning, N. Djilali, Three-dimensional computational analysis of transport phenomena in a PEM fuel cell – a parametric study, J. Power Sources 124 (2003) 440.

[10] T. Berning, N. Djilali, A 3D, multiphase, multicomponent model of the cathode and anode of a PEM fuel cell, J. Electrochem. Soc. 150 (2003) A1589–A1598.

[11] T. Berning, D.M. Lu, N. Djilali, Three-dimensional computational analysis of transport phenomena in a PEM fuel cell, J. Power Sources 106 (2002) 284–294.

[12] D. Natarajan, T.V. Nguyen, Three-dimensional effects of liquid water flooding in the cathode of a PEM fuel cell, J. Power Sources 115 (2003) 66–80.

[13] P.T. Nguyen, T. Berning, N. Djilali, Computational model of a PEM fuel cell with serpentine gas flow channels, J. Power Sources 130 (2004) 149.

[14] S. Shimpalee, S. Greenway, D. Spruckler, J.W. Van Zee, Predicting water and current distribution in a commercial-size PEMFC, J. Power Sources 135 (2004) 79–87.

[15] B. Sivertsen, N. Djilali, CFD based modelling of proton exchange membrane fuel cells, J. Power Sources 141 (2005) 65–78.

[16] S. Um, C.Y. Wang, Three-dimensional analysis of transport and electrochemical reactions in polymer electrolyte fuel cells, J. Power Sources 125 (2004) 40–51.

[17] L. Wang, H. Liu, Performance studies of PEM fuel cells with inter-digitated flow fields, J. Power Sources 134 (2004) 185–196.

[18] Z.H. Wang, C.Y. Wang, K.S. Chen, Two-phase flow and transport in the air cathode of proton exchange membrane fuel cells, J. Power Sources 94 (2001) 40–50.

[19] L. You, H. Liu, A two-phase flow and transport model for the cathode of PEM fuel cells, Int. J. Heat Mass Transf. 45 (2002) 2277–2287.

[20] G.F. McLean, Apparatus of high power density fuel cell layer with micro for connecting to an external load, US Patent 6 864 010 (2005).

[21] G.F. McLean, Apparatus of high power density fuel cell layer with micro structured components, WO03067693 (2003).

[22] G.F. McLean, Electrochemical cell, US Patent 6 872 287, 2005.

[23] S. Litster, G. McLean, PEM fuel cell electrodes, J. Power Sources 130 (2003) 61–76.

[24] M. Kaufman, Principles of Thermodynamics, Marcel Dekker, Inc., New York, 2002.

[25] W. Kast, C.-R. Hohenthanner, Mass transfer within the gas-phase of porous media, Int. J. Heat Mass Transf. 43 (2000) 807–823.

[26] M.J. Lampinen, M. Fomino, Analysis of free energy and entropy changes for half-cell reactions, J. Electrochem. Soc. 140 (1993) 3537–3546.

[27] D.M. Bernardi, M.W. Verbrugge, A mathematical model of the solid–polymer–electrolyte fuel cell, J. Electrochem. Soc. 139 (1992) 2477–2491.

[28] N.V. Suryanarayana, Engineering Heat Transfer, West Publishing Company, 1995.

[29] E.L. Cussler, DIFFUSION-Mass Transfer in Fluid Systems, Cambridge University Press, New York, 1997.

[30] M. Fishenden, O.A. Saunders, An Introduction to Heat Transfer, Oxford University Press, Oxford, 1950.

[31] T. Fujii, H. Imura, Natural-convection heat transfer from a plate with arbitrary inclination, Int. J. Heat Mass Transf. 15 (1972) 755–767.

[32] I. Martorell, J. Herrero, F.X. Grau, Natural convection from narrow horizontal plates at moderate Rayleigh numbers, Int. J. Heat Mass Transf. 46 (2003) 2389–2402.

[33] S. Pretot, B. Zeghmati, G. Le Palec, Theoretical and experimental study of natural convection on a horizontal plate, Appl. Therm. Eng. 20 (2000) 873–891.

[34] E.M. Sparrow, C.K. Carlson, Local and average natural convection Nusselt numbers for a uniformly heated, shrouded or unshrouded horizontal plate, Int. J. Heat Mass Transf. 29 (1986) 369–379.